Lattice Boltzmann simulation to study multiple bubble dynamics

Amit Gupta, Ranganathan Kumar *

Department of Mechanical, Materials and Aerospace Engineering, University of Central Florida, 4000 Central Florida Blvd., Room 307, Building 40, Orlando, FL 32816, United States

ARTICLE INFO

ABSTRACT

Lattice Boltzmann method (LBM) has been used in this study to understand the behavior of bubble motion and bubble coalescence in liquids. Highly isotropic gradient vectors have been obtained on a lattice for two-phase simulations using LBM. For a fully periodic domain, bubble dynamics and shape for a single bubble and multiple bubbles are dependent on Eotvos number, Reynolds number and Morton number. For single bubble simulations, computations were done for high Eotvos and low to moderate Reynolds numbers, and the results are matched with the experimentally quantified flow visualization chart. The drag coefficient for single bubble motion under buoyancy for both two- and three-dimensional simulations compares well with existing correlations. For multiple bubbles, the bubble dynamics is dictated by the vortex pattern of the leading bubble, which allows the bubbles to coalesce. Coalescence can be described as a three stage process: collision; drainage of the liquid film between adjacent bubbles to a critical thickness; and rupture of this thin film of liquid. Such simulations have also been run for different configurations of the initial bubble distribution for both in-line and staggered bubble configuration to show the effect of vortex shedding on the oscillatory motion of the bubbles and subsequent coalescence.

© 2008 Elsevier Ltd. All rights reserved.

1. Introduction

Boiling and two-phase flow situations are of major importance in industrial applications. Micro- and mini-channels are very commonly used these days in residential air-conditioners and thin compact evaporators that are being used in automotive and aerospace industries. The flow topology in such channels needs to be understood well for development of mechanistic models. Although the two-fluid technology has progressed significantly, there is little precedence describing the interfacial forces, heat and mass transfer in difficult transition flow regimes. In the slug and churn-turbulent regimes, where all types of interfaces exist, it is difficult to develop continuum transport equations and closure models for each phase, in particular the vapor phase which exists in different forms and shapes. For example, a bubble can be spherical, distorted, confined and/or elongated. The behavior of bubbles and slugs in an infinite medium depends on several parameters such as Reynolds number (Re), Eotvos number (Eo) and Morton number (Mo). There are empirical correlations that exist for terminal velocity and drag coefficient in terms of these non-dimensional parameters [1–3]. Earlier computational work in this field of bubble dynamics has been directed towards flow separation at a smooth free surface of a bubble in a quiescent liquid at moderate Reynolds numbers using body-fitted coordinates in which the density and viscosity of the vapor were neglected in comparison to that of the liquid

[4]. More recently, Esmaeeli and Tryggvason [5,6] conducted two- and three-dimensional simulations of buoyant bubbles in periodic domains for a range of low to moderate Reynolds numbers using their hybrid method. They found that a regular array of (slightly perturbed) bubbles is an unstable configuration that eventually leads to an asymmetrical arrangement. Sankaranarayanan et al. [7] have conducted single bubble simulations using an implicit formulation of LBM. Their simulations were conducted for $1 < Eo < 10$ and $Re > 100$. However, a detailed computational study into the dynamics of bubble collision and coalescence in a high pressure and low liquid-to-vapor density ratio system has not been undertaken where the Reynolds number is low and the Eo can be of $O(100)$. In LBM, the interfaces in different shapes occur naturally without having to be tracked as in averaged Navier–Stokes equations. This type of representation would encompass the various bubble regimes. Thus, it is important to focus on the fundamental understanding of the flow topology around single bubbles and the coalesced bubbles and rely less on empirical correlations or closure relations for the averaged Navier–Stokes equation. In this paper, the microscopic physics of bubble motion and shape evolution for very dilute single- and multiple bubble suspensions are studied for the range of $1 < Re < 100$ by conducting two- and three-dimensional simulations in a fully periodic domain. The effect of periodicity on bubble dynamics has been minimized by considering a long computational domain in the direction of rise of the bubble.

The objectives of this work are to (a) develop a method to determine the bubble interfaces using density gradients using Boltzmann's equation; (b) track the bubble movement for in-line and

Nomenclature

$\mathbf{a}$	acceleration, m/s^2
a	index for velocity–space discretization
c	lattice unit length, m
c_s	speed of sound, m/s
C_D	drag coefficient
d	diameter of the bubble, m
D	diameter of the spherical cap, m
$\mathbf{e}_i$	lattice speed of particles moving in direction i, m/s
Eo	Eotvos number
f	particle distribution function
$\mathbf{g}$	acceleration due to gravity, m/s^2
g_{ij}	interaction strength between components i and j
G	Green's function
m	molecular mass
Mo	Morton number
N	number of links at each lattice point
p	pressure, N/m^2
$\mathbf{p}$	momentum, kg-m/s
r	radius of the bubble, m
Re	Reynolds number
s	curvature of the stagnation point
S	number of phases
t	time, s
$\mathbf{u}$	velocity vector, m/s
U	velocity in the rise direction, m/s
V	interaction potential
We	Weber number

Greek symbols

$\delta_{\alpha\beta}$	Kronecker delta
v	kinematic viscosity, m^2/s
ρ	density, kg/m^3
σ	surface tension, N/m
τ	relaxation time
Φ	volume fraction
Ψ	effective mass function
Ω	collision operator

Subscripts

e	effective
i	index
b	bubble
L	liquid
sph	sphere
σ	phase index

Superscripts

*	non-dimensional quantities
eq	equilibrium
σ	phase index

staggered bubbles, determine the flow topology and bubble coalescence, and (c) to determine the terminal rise velocity and drag coefficient of single bubbles for various *Re*, *Eo* and *Mo* and compare with available experiments and correlations.

2. Methodology

In recent years, researchers have begun to use an alternative computational technique, called the lattice Boltzmann method (LBM), to simulate fluid flow as opposed to conventional methods based on solution of Navier–Stokes equations. The lattice Boltzmann method of simulating fluids has been proven to be an efficient algorithm, as it can handle flows in complex geometries, porous media, and in multiphase systems with relative ease. Frisch, Hasslacher and Pomeau [8] developed a simple cellular automaton that obeyed conservation laws at the microscopic level and was able to reproduce real fluid flows. This method was known as the lattice gas cellular automaton (LGCA) and was soon found to suffer from the lack of Galilean invariance, anomalous velocity dependence of the fluid pressure, statistical noise, high viscosity, exponential complexity and spurious invariants [9]. Later work by McNamara and Zanetti [10] helped circumvent two obstacles of LGCA, namely statistical noise and exponential complexity of the collision rule. This version of lattice Boltzmann evolved under the Bhatnagar–Gross–Krook (BGK) collision operator, and is the ultimate version of LBM in terms of simplicity, elegance and efficiency.

The Boltzmann's kinetic equation is a well established mathematical model of a fluid at the microscopic level which describes the evolution of the single particle distribution function. Unlike conventional schemes that are based on discretization of continuum based macroscopic equations, the lattice Boltzmann method models the microscopic and mesoscopic kinetic equations. The fundamental idea of LBM is to construct simplified kinetic models that incorporate the essential physics of microscopic or mesoscopic

processes so that the macroscopic averaged properties obey the desired macroscopic equations.

In multiphase flows, the standard technique is to use either the fluid-mixture or the two-fluid model. Each fluid is modeled by a modified Navier–Stokes (NS) equation, with extra source terms accounting for interfacial effects and forces. But the interface is dynamic, which is difficult to handle numerically with conventional methods. A mesoscopic method like LBM requires no empirical equations or correlations for closure of the extra source terms in the governing equations, and at the same time can yield detailed information about the physics of the flow around single or multiple bubbles. Moreover, in LBM, the interface is no longer a mathematical boundary; rather it is a post-processed quantity that can be detected by monitoring the variation in fluid densities.

2.1. LBM formulation

The evolution equation for the particle distribution function is very similar to the kinetic equation in lattice gas automata, given by

$$f_i(\mathbf{x} + \mathbf{e}_i \delta t, t + \delta t) = f_i(\mathbf{x}, t) + \Omega_i(f_i(\mathbf{x}, t)), \quad i = 0, 1, \ldots, N$$
$$\text{and } \Omega_i(f_i(\mathbf{x}, t)) = -\frac{f_i(\mathbf{x}, t) - f_i^{eq}(\mathbf{x}, t)}{\tau} \tag{1}$$

We have used the particular form of the collision operator with the single time relaxation approximation, also known as the lattice BGK (Bhatnagar–Gross–Krook) operator. This form of the collision operator leads to a differential equation of the form

$$\frac{\partial f_i}{\partial t} + \mathbf{e}_i \cdot \nabla f_i = -\frac{(f_i - f_i^{eq})}{\tau} \tag{2}$$

for the Boltzmann's kinetic equation. The macroscopic density per node and the macroscopic momentum flux are defined in terms of the particle distribution functions by

$$\rho = \sum_i f_i = \sum_i f_i^{eq}; \quad \rho \mathbf{u} = \sum_i f_i \mathbf{e}_i = \sum_i f_i^{eq} \mathbf{e}_i \tag{3}$$

The equilibrium distribution functions depend only on local density and velocity and they can be expressed in the following form:

$$f_i^{eq} = \frac{\rho - d_0}{b} + \frac{\rho D}{c^2 b}(\mathbf{e}_i \cdot \mathbf{u}) + \rho \frac{D(D+2)}{2c^4 b}(\mathbf{e}_i \mathbf{e}_i : \mathbf{u}\mathbf{u}) - \frac{\rho D}{2c^2 b}(\mathbf{u} \cdot \mathbf{u}),$$
$$f_0^{eq} = d_0 - \frac{\rho}{c^2}(\mathbf{u} \cdot \mathbf{u}) \tag{4}$$

where f_i^{eq} is the equilibrium distribution of particles moving in direction 'i', f_0^{eq} is the equilibrium distribution of rest particles, D is the dimension rank, b is the number of lattice directions, c is the lattice unit length, and d_0 is the average rest particle number [11]. Chen and Doolen [12] have shown Eq. (2) can be reduced to the Navier–Stokes equations in the low frequency, long wavelength limit using the Chapman–Enskog expansion together with Eq. (4). The resulting momentum equation is

$$\frac{\partial \rho}{\partial t} + \nabla \cdot \rho \mathbf{u} = 0 \tag{5a}$$

$$\rho \left(\frac{\partial \mathbf{u}}{\partial t} + \mathbf{u} \cdot \nabla \mathbf{u} \right) = -\nabla p + \upsilon \nabla^2 (\rho \mathbf{u}) + \upsilon \nabla \nabla \cdot (\rho \mathbf{u}) \tag{5b}$$

where $p = c_s^2 \rho$ and $\upsilon = c_s^2(\tau - 1/2)$. Thus the lattice Boltzmann's equation is able to bridge the gap between the microscopic fluid interactions and the macroscopic world as it yields Navier–Stokes equation in the low Mach number limit using the Chapman–Enskog expansion, and is second order accurate in space. In addition, $\tau > 1/2$ in order for viscosity to be positive.

2.1.1. Multiphase models in LBM

Numerous methods have been used by researchers over the past decade to conduct multiphase simulations using LBM. These include the model proposed by Rothman and Keller or better known as the R–K model [13], where the two-fluids are denoted by different colors. In this model, phase separation is induced by the repulsive interaction based on the color gradient. The R–K model was originally meant for lattice gas simulations. Grunau et al. [14] introduced some free parameters in this model.

The lattice Boltzmann implementation was first introduced by Shan and Chen [15]. In Shan–Chen's (S–C) model, the multiple phases were simulated by introducing non-local interactions between particles at each lattice site, thereby introducing spurious currents at the interface. Hou et al. [16] in one of the earliest works on multiphase LBM studied the Rothman–Keller (RK) and the Shan–Chen (SC) models. Their simulations were done for a static bubble with the ideal equation of state and in a static medium. They showed that the SC model is a major improvement over the RK model. This static bubble test has since then been used as a benchmark for conducting multiphase simulations using LBM. Yang et al. [17] used the SC model for their LB simulations and have qualitatively proved that results from LBM are very similar to experimental observations for saturated pool boiling. Sankaranarayanan et al. [7] proposed closures for drag and virtual mass terms that appear in two-fluid models through simulations performed using an implicit LBM using the SC model to simulate the liquid–vapor interaction. Later, Lee and Fischer [18] devised a new approach by which the spurious currents at the interface could be greatly minimized.

Swift et al. [19] proposed the "free-energy" approach. In this model, unlike the S–C model, the local momentum conservation was satisfied. Recent applications of this model have been focused towards development of methods that could simulate high density ratios for the liquid–vapor mixture. Inamuro et al. [20] used the projection method together with Swift's free-energy model to deal with immiscible fluids with large density ratios. In their work, they demonstrated the applicability of the algorithm developed for the

case of droplet collisions surrounded by a lighter fluid. In another work, Inamuro et al. [21] conducted simulations for bubbly flows with large density ratios using the projection method. In addition, recent work has also been concentrated on the lattice Boltzmann simulations of multiphase flows with high density ratios [22,23] to study liquid–gas systems.

Takada et al. [24], in their work on bubble motion under gravity, developed a 3-D version of the binary fluid model that introduces a free energy function into the LBE. Their results proved that LBM is suitable for numerical analysis of bubble motion under gravity. Their simulations were conducted using a two-dimensional hexagonal lattice arrangement. They have also shown bubble migration towards the center of the channel for wall-driven shear flows. In more extended simulations, they demonstrated binary bubble coalescence and the stages involved in the process. However, Swift's model suffers from the lack of Galilean invariance.

More recently, Kurtoglo and Lin [25] used the phase-field method to assess its applicability to single bubble dynamics. But not much attention was given to the study of bubble coalescence
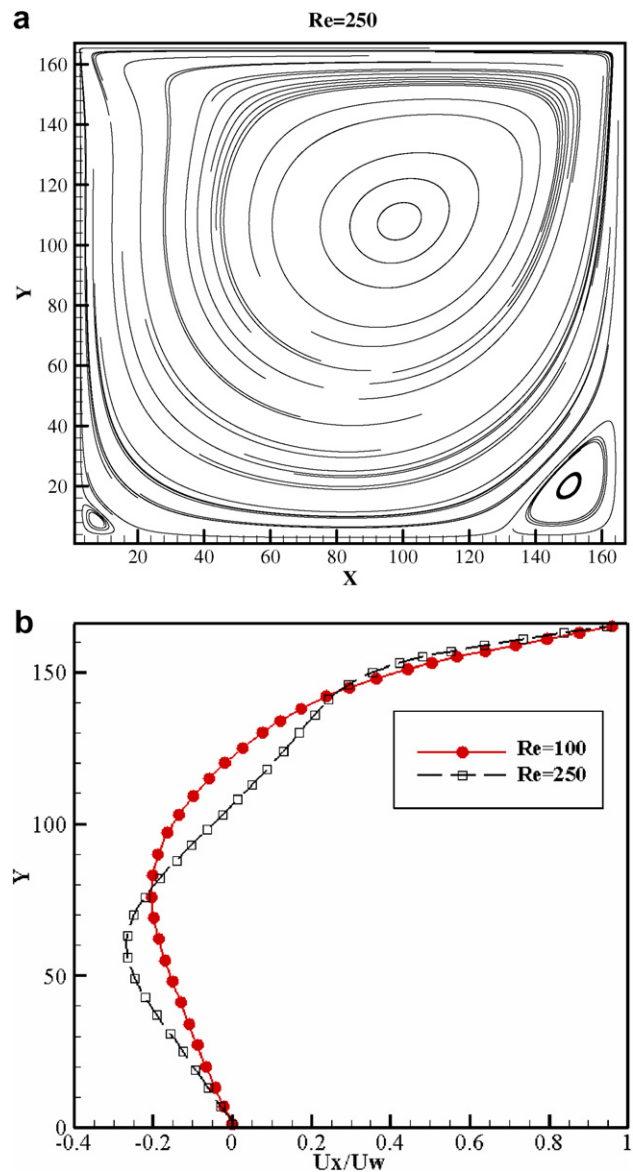

Fig. 1. Results for the 2-D lid-driven cavity simulation obtained using LBM showing (a) streamlines at a Reynolds number of 250, and (b) center-line velocity for two different Re values of 100 and 250.
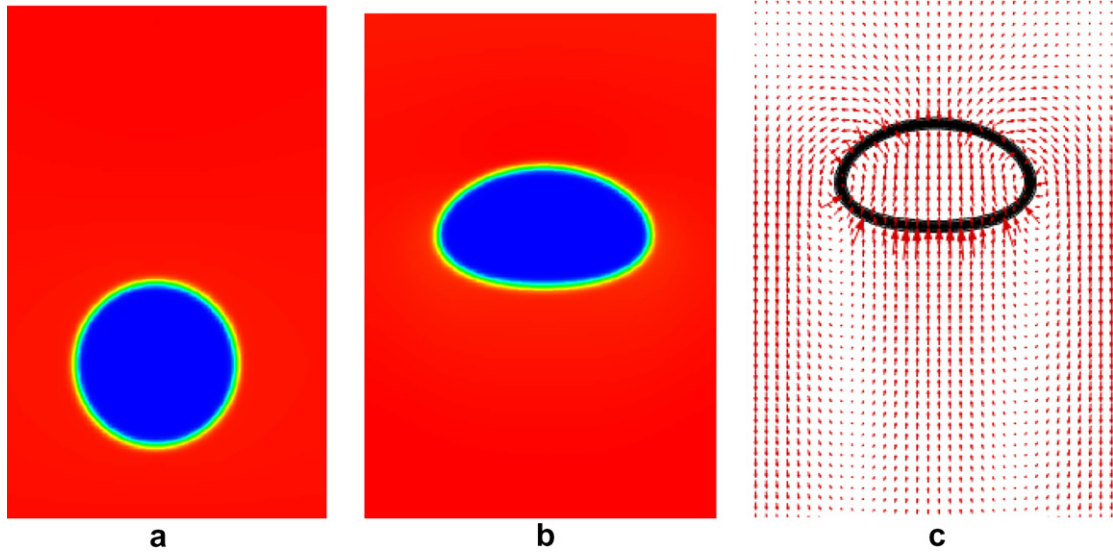
Fig. 2. Bubble shape evolution under gravity at an Eotvos number of 10.7. The time instants are at (a) initial condition, and (b) $t^* = 10.6$ (c) velocity vectors around the bubble as it forms an ellipsoidal shape at steady state.

behavior, and in particular transition behavior from bubbly to slug flow regime. Through this work, we aim to establish the mechanism for bubble coalescence in the presence of gravity using isothermal LBM. In this work, the S–C model has been used extensively to study isothermal flow behavior of immiscible components and multiple phases. The S–C model is described below.

2.1.2. S–C model for multiple phases and components

Shan and Chen [15] in their work proposed a lattice Boltzmann based model that could simulate multiple phases and components. They incorporated non-local interactions amongst particles to simulate multiple component fluids. The interaction potential between components σ and $\bar{\sigma}$ was defined as

$$V(\mathbf{x}, \mathbf{x}') = G_{\sigma\bar{\sigma}}(\mathbf{x}, \mathbf{x}')\psi^\sigma(\mathbf{x})\psi^{\bar{\sigma}}(\mathbf{x}') \qquad (6)$$

where $G_{\sigma\bar{\sigma}}(\mathbf{x}, \mathbf{x}')$ is the Green's function. The quantity ψ^σ is the "effective mass". If only nearest neighbor interactions were considered, then

$$G_{\sigma\bar{\sigma}}(\mathbf{x}, \mathbf{x}') = \begin{cases} 0; |\mathbf{x} - \mathbf{x}'| > c \\ G_{\sigma\bar{\sigma}}; |\mathbf{x} - \mathbf{x}'| = c \end{cases} \qquad (7)$$

The magnitude of $G_{\sigma\bar{\sigma}}$ controls the strength of the interaction between components σ and $\bar{\sigma}$, while its sign determines whether the interaction is attractive or repulsive.

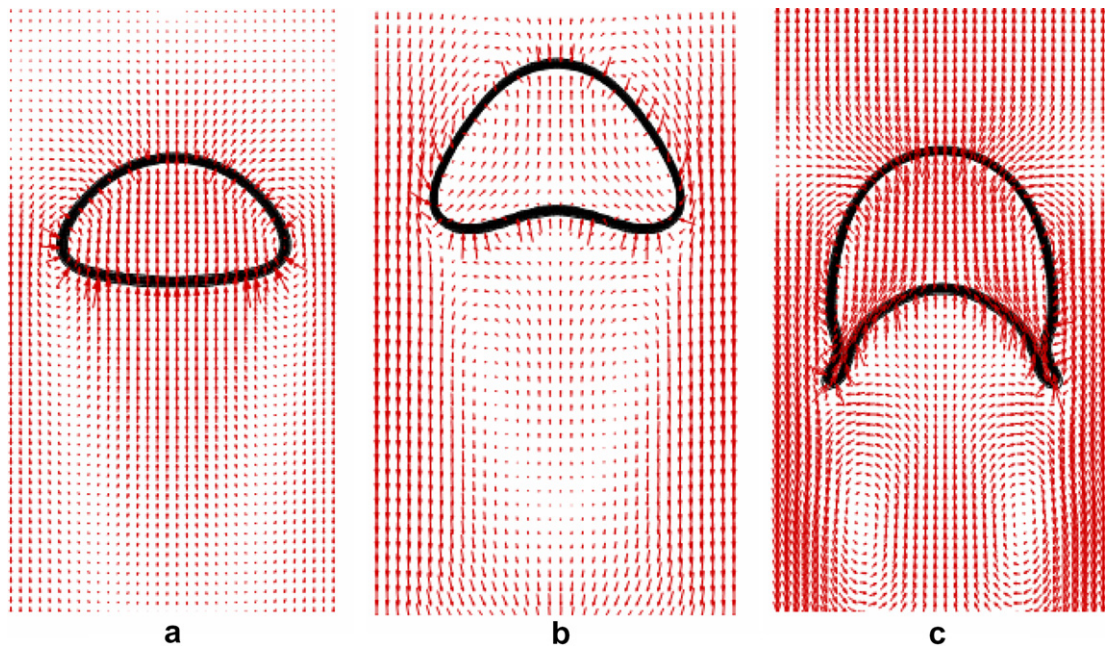This form of the potential gives the rate of net momentum change at each lattice site to be

Fig. 3. Bubble deformation as computed using LBM for different sizes of the initial bubble. Density ratio is 2.66 for all the simulations. The Eotvos number for each case is (a) Eo = 37.2, (b) Eo = 74.5 and (c) Eo = 297.2.

Table 1
Parameters for single bubble simulations using LBM[*]

	d_e	Eo	Mo	Re	Shape
(a)	52	5.03	3.2×10^{-4}	17.22	Oblate ellipsoid
(b)	56	6.37	4.15×10^{-4}	18.82	Oblate ellipsoid
(c)	60	7.76	4.94×10^{-4}	21.1	Oblate ellipsoid
(d)	40	1.56	7.36×10^{-4}	3.74	Spherical
(e)	34	0.26	9.27×10^{-4}	0.27	Spherical
(f)	40	3.13	1.47×10^{-3}	6.72	Oblate ellipsoid
(g)	48	7.59	1.75×10^{-3}	15.09	Oblate ellipsoid
(h)	30	8.76	1.86×10^{-3}	18.0	Oblate ellipsoid
(i)	44	7.03	2.35×10^{-3}	13.29	Oblate ellipsoid
(j)	40	6.94	4.0×10^{-3}	11.26	Oblate ellipsoid
(k)	48	18.97	4.38×10^{-3}	27.04	Oblate ellipsoid cap
(l)	52	23.74	5.3×10^{-3}	31.2	Oblate ellipsoid cap
(m)	44	17.57	5.86×10^{-3}	23.65	Oblate ellipsoid
(n)	30	.64	7.06×10^{-3}	0.39	Spherical
(o)	40	15.65	7.36×10^{-3}	20.86	Oblate ellipsoid
(p)	56	32.18	8.46×10^{-3}	37.3	Oblate ellipsoid cap
(q)	36	7.25	8.57×10^{-3}	8.64	Oblate ellipsoid
(r)	40	17.35	1.00×10^{-2}	20.58	Oblate ellipsoid
(s)	24	9.02	1.19×10^{-2}	10.3	Oblate ellipsoid
(t)	40	26.03	1.50×10^{-2}	26.64	Oblate ellipsoid
(u)	30	6.14	1.56×10^{-2}	5.58	Oblate ellipsoid
(v)	30	1.6	1.77×10^{-2}	0.96	Spherical
(w)	34	5.27	1.85×10^{-2}	4.65	Oblate ellipsoid
(x)	36	18.13	2.14×10^{-2}	17.39	Oblate ellipsoid cap
(y)	30	3.21	3.53×10^{-2}	1.85	Spherical

[*] For all cases, $\rho_L/\rho_g = 2.66$.

$$\frac{d\mathbf{p}^\sigma}{dt}(\mathbf{x}) = -\psi^\sigma(\mathbf{x}) \sum_{\bar{\sigma}=1}^{S} G_{\sigma\bar{\sigma}} \sum_{a=0}^{b} \psi^{\bar{\sigma}}(\mathbf{x} + \mathbf{e}_a)\mathbf{e}_a \tag{8}$$

Therefore, this change in momentum is applied at each lattice site in the equilibrium distribution function before the collision, as shown by Buick and Greated [26]:

$$\rho^\sigma \mathbf{u}^\sigma = \rho^\sigma \mathbf{u} + \tau^\sigma \frac{d\mathbf{p}^\sigma}{dt}(\mathbf{x}) \tag{9a}$$

where

$$\rho^\sigma = m^\sigma f^\sigma(\mathbf{x}) \tag{9b}$$

is the mass density of the σth component and

$$\mathbf{u} = \frac{\sum_\sigma^S m^\sigma \sum_a f_a^\sigma \mathbf{e}_a/\tau^\sigma}{\sum_\sigma^S m^\sigma \sum_a f_a^\sigma/\tau^\sigma} \tag{9c}$$

and

$$f^\sigma(\mathbf{x}) = \sum_a f_a^\sigma \tag{9d}$$

3. Results and discussion

Simulations were done for single-component single-phase flows to assess the validity of the lattice Boltzmann method. A 2-D lid-driven cavity flow for two Reynolds numbers of 100 and
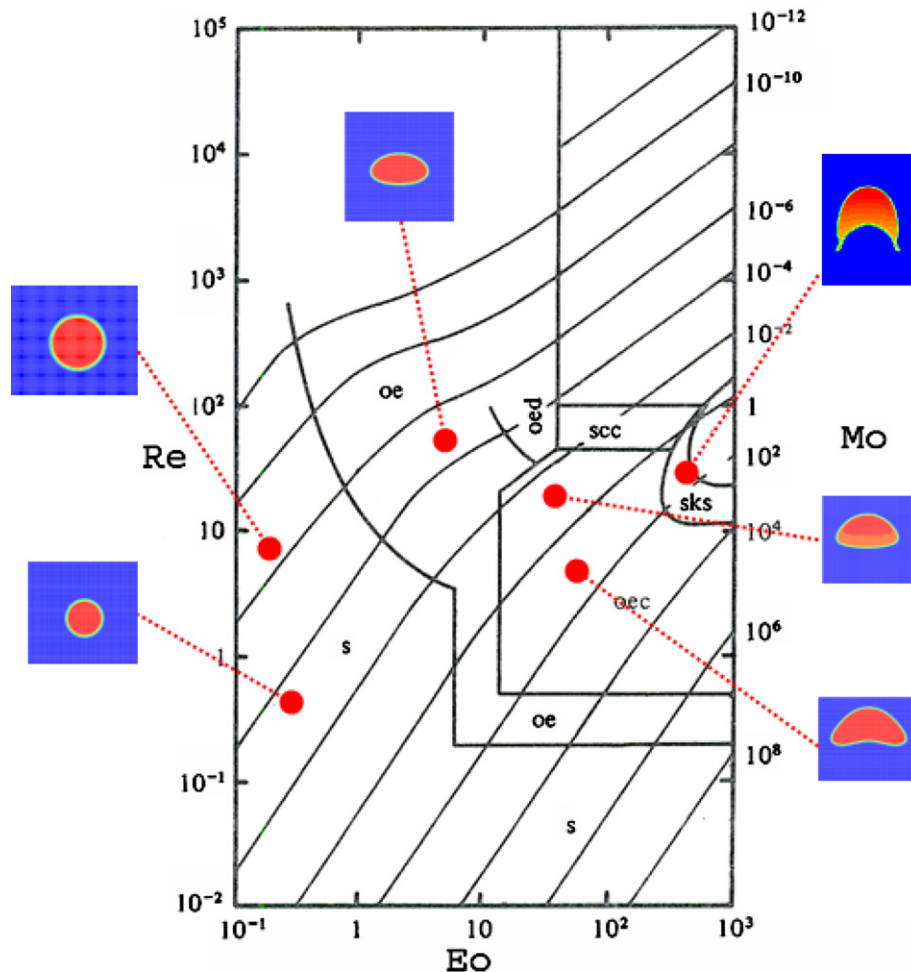

Fig. 4. Shape regime map for isolated bubbles in liquids taken from [1]. The pictures in the inset show the results of the numerical simulations using LBM; s, spherical; oe, oblate ellipsoidal; oed, oblate ellipsoidal disk-like and wobbling; oec, oblate ellipsoid cap; scc, spherical cap with closed wake,; sks, skirted with smooth steady wake.

250 was carried out. The extrapolation scheme proposed by Chen and Martinez [27] has been used for the particle distribution functions at the walls. The streamlines for Re = 250 is shown in Fig. 1a. A comparison of the horizontal velocity in the cavity along the vertical centerline is shown in Fig. 1b for Re = 100 and Re = 250. The flow velocity and streamlines are in good agreement with results published in [27].

Multiphase simulations using LBM were performed next. The most important parameters in the study of bubble motion are Eotvos number, $Eo = g\Delta\rho d_e^2/\sigma$, Morton number, $Mo = g\rho_L^2\Delta\rho v^4/\sigma^3$, Reynolds number, $Re = U_b d_e/v$ and Weber number, $We = \rho_L U_b^2 d_e/\sigma$. Grace [1] has shown the relationship of Eotvos number with Reynolds number for a wide range of Morton numbers. Weber number is a ratio of the dynamic pressure ($\sim \rho_L U_b^2$) to the surface tension pressure ($\sim\sigma/d_e$). For $We \ll 1$, bubbles maintain a spherical shape throughout the flow domain. These parameters have been used in this study to record and observe bubble shapes and flow regimes.
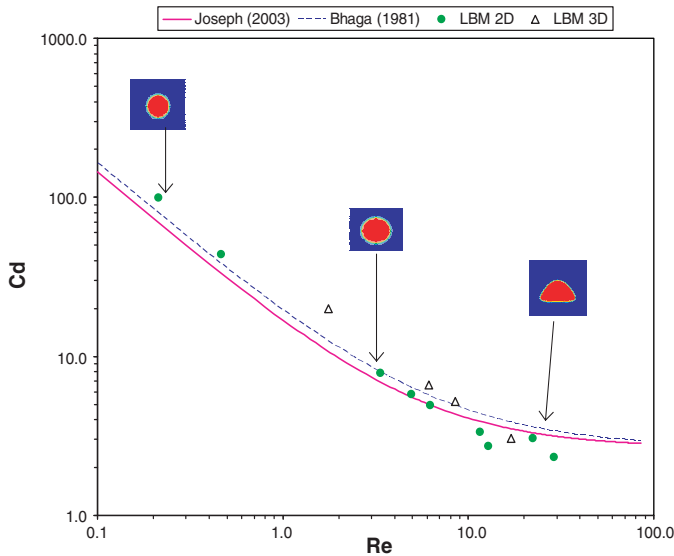
Multiphase simulations in LBM were initially conducted with static bubble tests to generate a good initial condition with one bubble in a fully periodic domain for both 2-D and 3-D simulations. The nearest neighbor SC model as explained by Yuan and Schaefer [28] has been used in which the next-nearest neighbor is also used in the force discretization. Accordingly, Eq. (7) is modified to account for the nearest and second nearest neighbors as

$$G_{\sigma\bar{\sigma}}(\mathbf{x}, \mathbf{x}') = \begin{cases} g; & |\mathbf{x} - \mathbf{x}'| = 1 \\ g/4; & |\mathbf{x} - \mathbf{x}'| = \sqrt{2} \\ 0; & \text{otherwise} \end{cases} \tag{10}$$

This leads to a non-ideal equation of state that is given by

$$p = c_S^2\rho + \frac{3}{2}g\Psi^2(\rho) \tag{11a}$$

in 2-D for the D2Q9 lattice and

$$p = c_S^2\rho + 3g\Psi^2(\rho) \tag{11b}$$

in 3-D for the D3Q19 lattice arrangement. $c_S = 1/\sqrt{3}$ is the speed of sound in lattice units. It should be noted here that if there is no interaction amongst the same kind of fluid, then the equation of state would reduce to the ideal gas equation of state given by $p = c_S^2\rho$. The 'effective mass' function, Ψ, used for the liquid is the same as proposed by [15], given by

$$\Psi(\rho) = \rho_0[1 - \exp(-\rho/\rho_0)] \tag{12}$$

This leads to a value of the critical interaction strength to be $g_{crit} = -\frac{4}{9\rho_0}$ (2-D) and $g_{crit} = -\frac{2}{9\rho_0}$ (3-D). Any value of the interaction strength below g_{crit} would result in phase separation of the liquid phase. In most simulation results described below, ρ_0 = 1 unless otherwise specified. For the vapor phase, ψ is set equal to ρ. The lighter fluid obeys an ideal equation of state, because g_{11} = 0.

Two-phase simulations are started by conducting a static bubble test, in which a single bubble is equilibrated in a fully periodic domain initially. An interface of thickness close to three lattice units is formed at the surface of the bubble because of the sudden transition in the density of the fluid-mixture. This value of the interface thickness is the same as reported by Hou et al. [16].

The static bubble test yields a good initial guess for the density and pressure distribution in the domain for the multiphase simulation, even before gravity is introduced. After letting the bubble(s) equilibrate for a long time in the domain, a steady state is achieved, and gravity is switched on. The gravitational force is in the negative vertical direction. Sankaranarayanan et al. [7] have suggested

Fig. 5. The drag coefficient as computed for single bubbles from two- and three-dimensional lattice Boltzmann simulations at different Reynolds numbers compared with the correlation in Bhaga and Weber [2] and the theoretical solution of Joseph [32]. Pictures in the inset show bubble deformation at different Reynolds numbers.
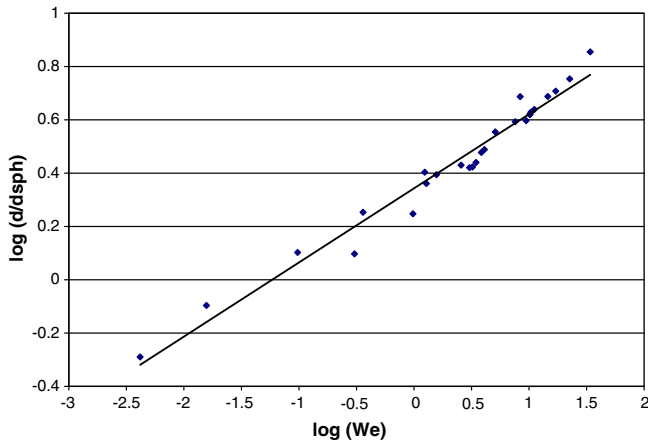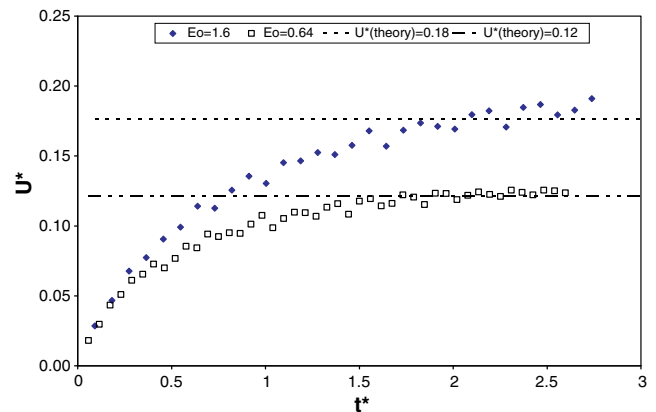

Fig. 6. Plot of the $\log(d_e/d_{sph})$ versus $\log(We)$. A large value of the diameter ratio implies a higher deviation of the bubble from pure spherical shape.

Fig. 7. Non-dimensional rise velocity as a function of time compared with the potential flow solution of Joseph [32] for bubbles with very low Weber number (i.e. $We \ll 1$). The symbols show current LBM results, and the dotted lines show the theoretical predicted value.

that this external force can be introduced into the force equation using the expression

$$\mathbf{a}_{\text{ext}} = \mathbf{g}\left(1 - \frac{\langle \rho \rangle}{\rho}\right) \tag{13}$$

where ρ is the mixture number density at the node of interest and $\langle \rho \rangle$ is the average number density of the mixture in the entire domain. This choice ensures that the average value of the external force is zero in the periodic domain, and hence the mass-average velocity of the mixture is constant.

To capture bubble motion for a long enough time and to achieve steady state, a two-dimensional domain of with 100×300 lattice units and periodic boundary conditions was selected and a new static bubble was created and released from rest to rise under buoyancy. The number of lattice nodes in either direction was selected such that the effect of the trailing wake on the bubble motion was negligible. Fig. 2a and b shows bubble snapshots at different instants of time as the bubble shape evolves under the influence of gravity. Time has been non-dimensionalized as $t^* = t/\sqrt{d_e/g}$. The simulation was done at $Eo = 10.7$ and $Mo = 2.38 \times 10^{-3}$. At this Eotvos number, the bubble shape changes from spherical to an ellipsoid. Liquid-to-vapor density ratio is 2.66 and weighting factors as suggested by Shan [29] for sixth order isotropic tensor are used for the fluid–fluid interaction to minimize the magnitude of the spurious currents. Using this form of the force discretization leads to an equation of state for the liquid to be of the form

$$p = c_s^2 \rho + \frac{15}{8} g \Psi^2(\rho) \tag{14}$$

The interaction strengths were taken to be $g_{11} = 0$, $g_{22} = -0.3$, $g_{12} = 0.15$. The velocity vectors around the bubble are shown in Fig. 2c. The presence of closed wakes behind the bubble is clear. The bubble forms an oblate ellipsoidal cap as has been discussed
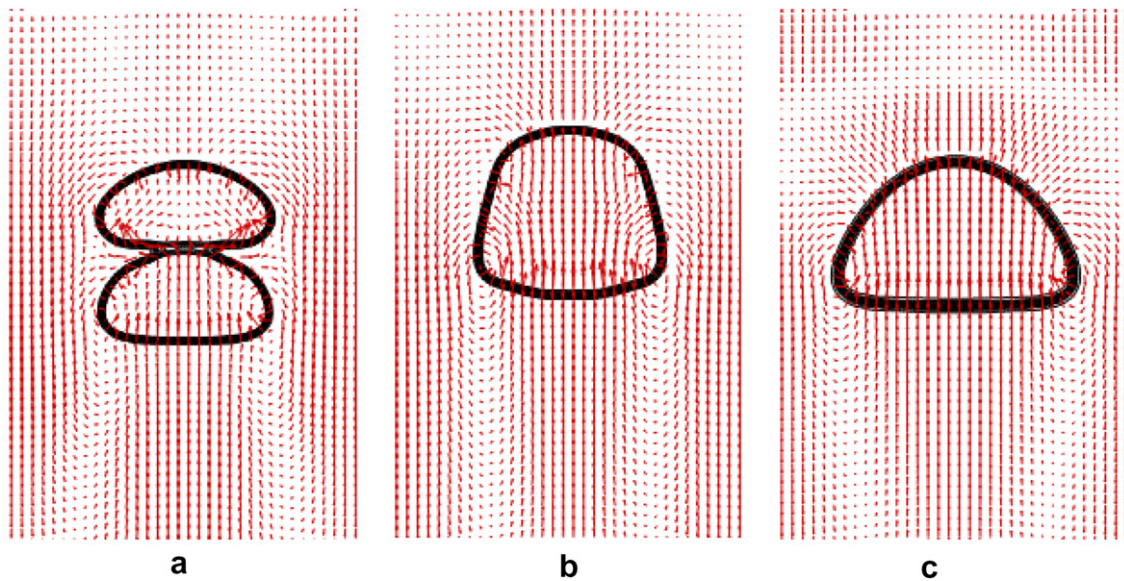

Fig. 8. Bubble coalescence for a flow situation with two bubbles of equal size of diameter 40 lattice units separated by center to center distance of 2.5d initially. Bubbles touch at (a) $t^* = 21.9$; (b) bubbles coalesce at $t^* = 22.62$ to form a bell-shaped blob; (c) bubble attains a spherical cap shape at $t^* = 27.6$.
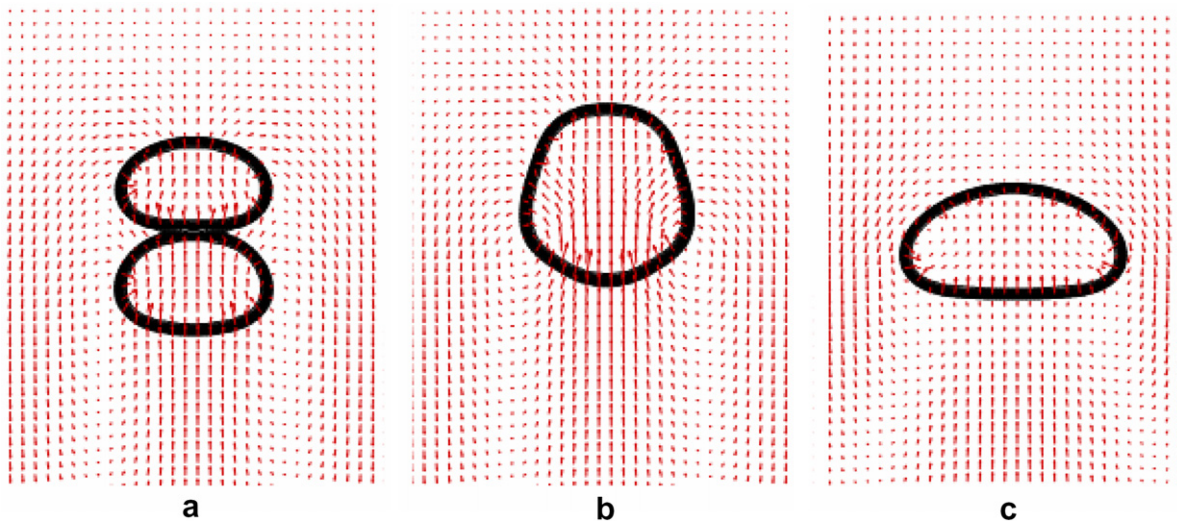

Fig. 9. Bubble coalescence for a flow situation with two bubbles of equal size of diameter 30 lattice units separated by center to center distance of 2d initially. Bubbles touch at (a) $t^* = 11.0$; (b) bubbles coalesce at $t^* = 11.84$ to form a bell-shaped blob; (c) bubble attains an oblate ellipsoidal shape at $t^* = 20.4$.

by Bhaga and Weber [2], who did experiments to study the wake behavior behind moving bubbles with hydrogen bubble tracer technique. Fig. 3 shows a comparison of the 2-D single bubble flow behavior and the bubble shape deformation/change as a function of Eotvos and Morton numbers. The number of lattice nodes used is 100×300. It is clear that as the Eotvos number increases, the bubble deformation and wake characteristics change very dramatically. The parameters for the single bubble simulations are listed in Table 1. It can be seen that as the Eotvos number increases, the bubble shape changes from an ellipsoid (Fig. 3a) to a disk (Fig. 3b) and then for even higher Eotvos numbers, the bubble takes a skirt-like shape (Fig. 3c). These shapes correspond very well with the parameters provided in the chart created by Bhaga and Weber [2] and the numerical results of Tomiyama [30]. Fig. 4 shows the well-known bubble shape regime map constructed by [1] using flow visualization. For various Re and Eo, the bubbles were characterized as spher-

ical (s), oblate ellipsoid (oe), oblate ellipsoidal disk-like (oed), oblate ellipsoid cap (oec); spherical cap with closed wake (scc), and skirted (sks). Several cases were run using the current LBM for various Re, Eo and Mo as given in Table 1 and have been characterized as spherical, oblate ellipsoid and oblate ellipsoid cap bubbles. Six representative cases are plotted along with Grace's [1] regime map in Fig. 4. This figure shows that the current numerical simulation using LBM yields excellent quantitative and qualitative results for single bubble simulations. The shapes predicted in the current study are also found to match well with the bubble regime map given by [25].

3.1. Drag force and drag coefficient calculations

Most of the available correlations for drag have been developed for a single bubble in an infinite medium. However, the ideas can be extended to small tubes and channels for very small bubbles.
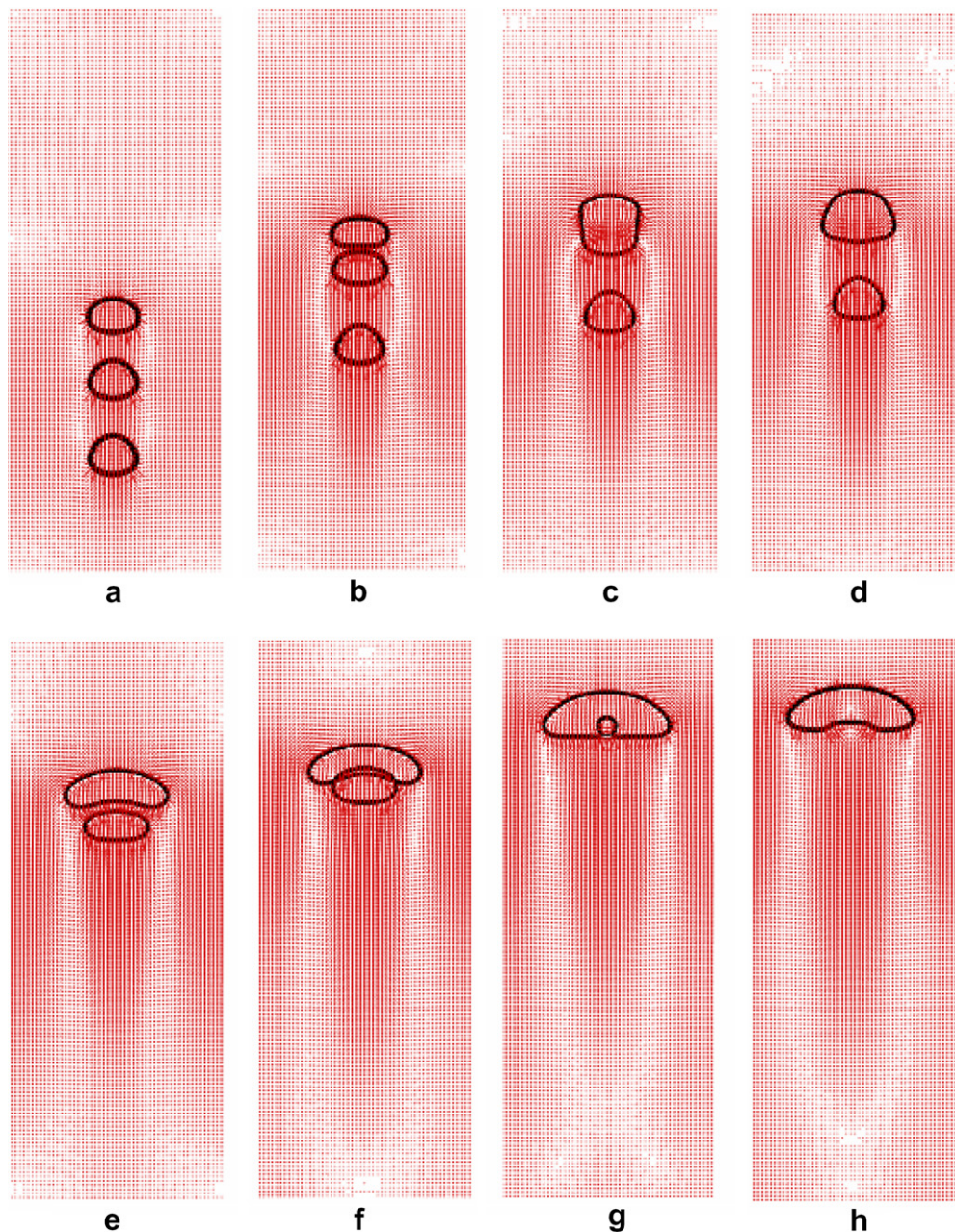

Fig. 10. Dynamics of three bubbles separated by a continuous liquid phase at $Eo = 2.88$ and $Mo = 2.71 \times 10^{-4}$. The domain is two-dimensional and divided into 150×400 lattice nodes. Bubbles are aligned vertically; (a) $t^* = 2.85$, (b) $t^* = 6.12$, (c) $t^* = 6.94$, (d) $t^* = 7.35$, (e) $t^* = 10.2$, (f) $t^* = 11.02$, (g) $t^* = 13.88$, and (h) $t^* = 14.29$.

For larger bubbles that are confined by the walls, the correlations may not be valid since the bubbles elongate with a spherical cap and a cylindrical tail [3]. In order to calculate the drag coefficient for a bubble in the dispersed field, the spherical equivalent size of the capped bubble is one that is widely considered. Even within the dispersed field, the bubbles go through distinct regimes and have different rise velocities. The rise velocity given as a function of the equivalent bubble diameter is an important component in the development of bubble drag models.

The bubble diameter at which the bubble ceases to be spherical is proportional to $d_{sph} = (\sigma/\Delta\rho g)^{0.5}$. This quantity simply comes from the force balance between the buoyancy and surface tension acting on the bubble. This can also be recast in terms of the parameter, Eotvos number, Eo, defined as $Eo = g\Delta\rho d_e^2/\sigma$. Tomiyama [30]

classified bubbles in several groups based on their Eo. For each field or group, he used a drag coefficient based on Eotvos and Morton number. Based on the proposed drag coefficient, he calculated the terminal rising velocities of single bubbles in stagnant liquids, and plotted Re vs. Eo for various Morton number to compare with available data. He classified the bubble shapes for $Mo < 10^{-6}$ into spherical and ellipsoidal (oblate spheroid, $Eo < 40$) and spherical cap ($Eo > 40$) with a flat rear surface. This is an effective approach in thin tubes if the flow regime is predominantly bubbly and slug flow. Zun [31] describes the intrinsic fluctuating bubble motion in terms of Eo, and reports that the magnitude of the fluctuation increases with Eotvos number. Using an interface tracking method, Tomiyama [30] predicted single bubble motion to determine the effect of Eotvos number. Their predicted velocity field indicates
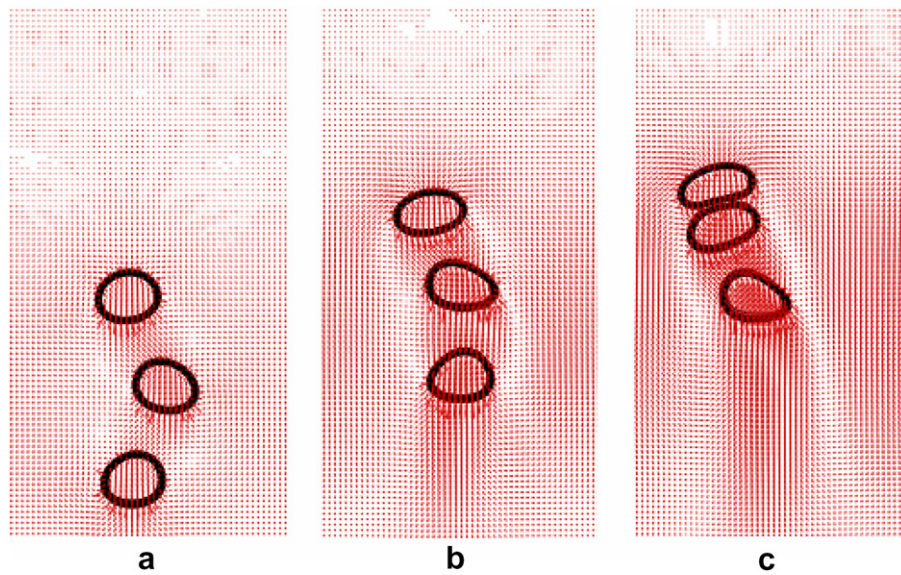

Fig. 11. Dynamics of three bubbles separated by a continuous liquid phase at $Eo = 3.04$ and $Mo = 3.16 \times 10^{-4}$. Bubbles are in staggered alignment with respect to the gravity vector; (a) $t^* = 1.84$, (b) $t^* = 4.9$, and (c) $t^* = 7.96$.
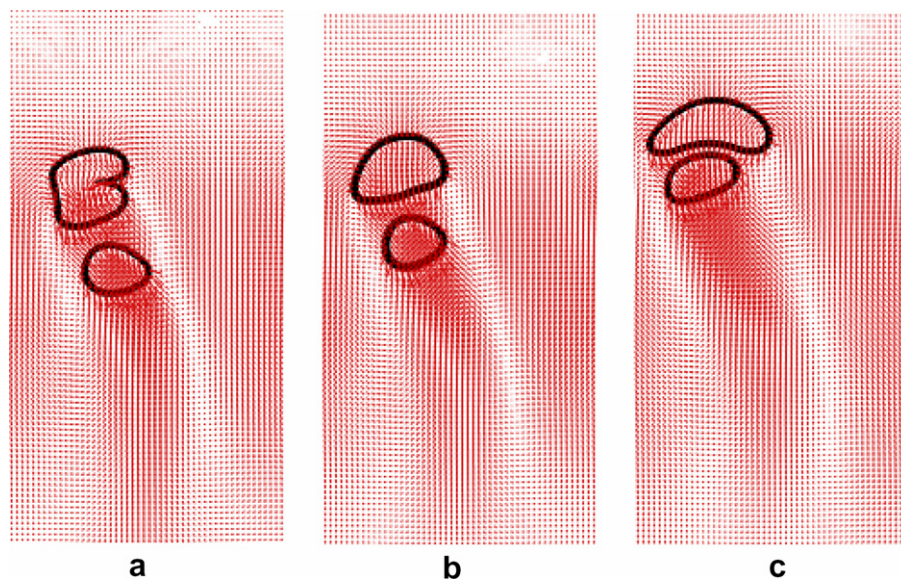

Fig. 12. Dynamics of three bubbles separated by a continuous liquid phase at $Eo = 3.04$ and $Mo = 3.16 \times 10^{-4}$. Bubbles are in staggered alignment with respect to the gravity vector; (a) $t^* = 8.57$, (b) $t^* = 9.19$, and (c) $t^* = 10.41$.

that the bubble fluctuation is closely related to the periodic vortex shedding, and Eo is the most appropriate parameter to define the lateral movement of the bubbles.

In our study, drag coefficient calculations were conducted using buoyancy-driven single bubble simulations at various void fractions for the same bubble diameter. The isolated bubble was simulated at low void fractions and the velocity of such a bubble was computed till it reached a steady value. Such calculations were done for various sizes of the 2-D and 3-D domain keeping the bubble diameter the same, and the Reynolds number for each void fraction was recorded. Subsequently, a log–log plot of Re vs. $1 - \Phi$, where Φ is the volume fraction of vapor in the domain was generated. Extrapolation of this curve in the limit of $\Phi \to 0$ gives the terminal Reynolds number for a given bubble size, from which terminal velocity can be determined.

The drag coefficient is obtained from a force balance and is given by $C_D = \frac{4}{3} \frac{\Delta\rho}{\rho_L} \frac{g d_e}{U_b^2}$ in 3-D and $C_D = \frac{\pi}{2} \frac{\Delta\rho}{\rho_L} \frac{g d_e}{U_b^2}$ in 2-D. The calculations for the drag coefficient have been compared to the correlation of Bhaga and Weber [2], in which the drag coefficient for fluids with high Morton numbers ($Mo > 4 \times 10^{-3}$) is said to obey the relationship

$$C_D = \left[(2.67)^{0.9} + \left(\frac{16}{Re} \right)^{0.9} \right]^{1/0.9} \qquad (15)$$

Results of the numerical computations have also been compared to the theoretically derived drag coefficient of Joseph [32], in which C_D is given by

$$C_D = 0.445 \left(6 + \frac{32}{Re} \right) \qquad (16)$$

These results are shown in Fig. 5. It is a well-known phenomena that spherical bubbles undergo a so-called hindered rise, as has been shown by [33], whereas the deformed bubbles (high Eo) are affected by the wake of preceding bubble, leading to a cooperative rise. It has also been pointed out in [33] that the Richardson–Zaki exponent for the case of essentially spherical bubbles in 3.6, indicating higher drag for such cases. The current results show the same trend where the drag coefficient is slightly over-predicted for low Re, but under-predicted at moderate Re. It is also observed that the primary difference between 2-D and 3-D bubble dynamics is in terms of the computed drag force. It is found that at low Reynolds numbers ($Re \leqslant 1$), the drag force for the 2-D bubble is less than what is calculated through 3-D dynamics (because of the hindered rise). As the Reynolds number is increased, the 3-D bubble dynamics formulation predicts a drag force that matches well with the theoretical and experimental correlations, as compared to the 2-D formulation. With the current explicit formulation of LBM, bubble Reynolds numbers are limited to O(100). This was mainly done to capture a wide range of Morton numbers.

Next, Weber number vs. effective bubble diameter is plotted in Fig. 6. The effective bubble diameter is non-dimensionalized using $d_{sph} = (\sigma/\Delta\rho g)^{0.5}$, which effectively yields $Eo^{1/2}$. This was done to study the bubble shape behavior as a function of the bubble diameter. When $We \ll 1$, the surface tension pressure dominates over the dynamic pressure, and hence the bubble shape remains purely spherical. Fig. 6 shows that for small effective bubble diameters, or small Eo, the Weber number is also small, and the shape is observed to be pure spherical. Bubble diameter increased with Weber number, resulting in a higher distortion in the bubble shape (see inset Fig. 5). This also indicates that the surface tension pressure can no longer hold the bubble as a sphere and hence the dynamic pressure of the bubble dominates, creating a highly distorted bubble. For the cases where the Weber number was small as compared to unity, terminal velocity calculations have been compared to the theoretically derived equation given by Joseph [32], which is derived from

the theory of potential flow for a spherical cap bubble. According to his work, such bubbles obey a dependence of the velocity on the fluid viscosity and the diameter of the spherical cap, and also the curvature at the stagnation point of the bubble. The terminal velocity is given by

$$\frac{U}{\sqrt{gD}} = \frac{-8\upsilon(1 + 8s)}{3\sqrt{gD^3}} + \frac{\sqrt{2}}{3} \left[1 - 2s - \frac{16s\sigma}{\rho gD^2} + \frac{32\upsilon^2}{gD^3}(1 + 8s)^2 \right]^{1/2} \qquad (17)$$

where 's' is the curvature at the stagnation point of the bubble, and is equal to zero for a perfectly spherical bubble. In the small Weber number limit, i.e. for $We \ll 1$, the expression can be simplified and written as

$$U^* = \frac{U}{\sqrt{gD}} = \frac{-8\upsilon}{3\sqrt{gD^3}} + \frac{\sqrt{2}}{3} \left[1 + \frac{32\upsilon^2}{gD^3} \right]^{1/2} \qquad (18)$$

Joseph [32] has called the non-dimensional form of the velocity as the Froude number. The non-dimensional velocity calculated through the code as the bubble attains a steady terminal velocity is shown in Fig. 7 for two cases of $Eo = 0.64$ and $Eo = 1.6$. The development of the rise velocities has been plotted as a function of the non-dimensional time, given as $t^* = t/\sqrt{d_e/g}$. The results show a perfect match of the computed velocity profile in the Stokes flow limit when compared to the derived non-dimensional velocity of [32].

3.2. Multi-bubble simulations

Simulations were also done for multiple vapor bubbles in a periodic domain. In a thin vertical rectangular channel, Jones and Zuber [34] observed that the slug regime seldom contains Taylor-type bubbles. Instead, the bubbles in the slug flow oscillated wildly from side to side and snakewise along the upward flow direction. They observed the Karman vortex street behavior by the entrained bubbles behind major voids using the high-speed motion pictures. Under the influence of the trailing vortex street, the nose of the elongated bubbles moved from side to side. Later from geometric considerations, Mishima and Hibiki [35] showed that the possibility of collisions and coalescence would increase if the maximum
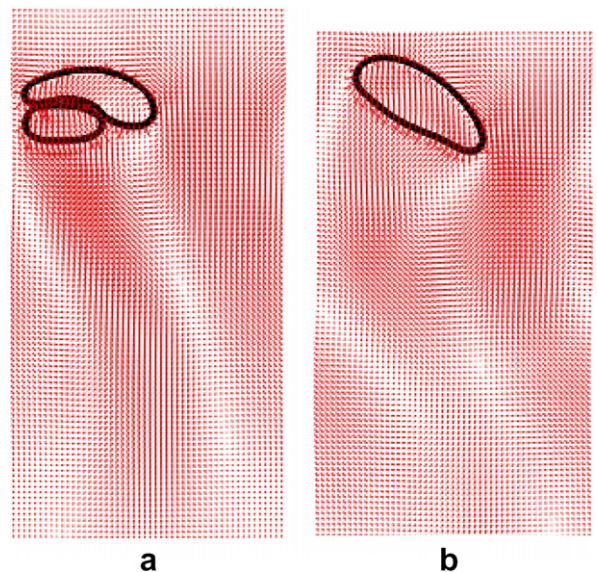

Fig. 13. Dynamics of three bubbles separated by a continuous liquid phase at $Eo = 3.04$ and $Mo = 3.16 \times 10^{-4}$. Bubbles are in staggered alignment with respect to the gravity vector. (a) $t^* = 11.64$, and (b) $t^* = 15.92$.
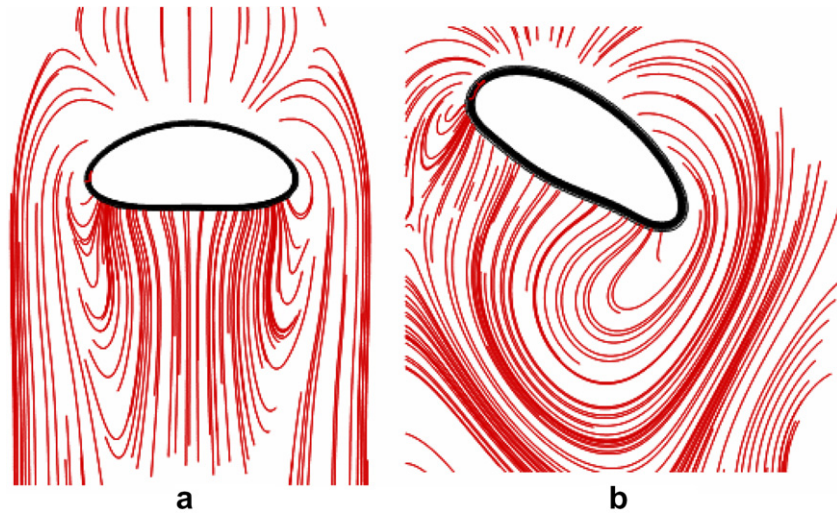
Fig. 14. Comparison of the streamlines around the bubble for the case of Figs. 10a and 11–13b. The flow field around (a) is symmetrical about the center axis unlike (b). This causes the bubble in (b) to oscillate as it moves upwards.

distance between two bubbles is less than the projected diameter of flat bubble. Esmaeeli and Tryggvason [5,6] show that a regular array of bubbles is an unstable arrangement when the bubbles are released from a slightly perturbed initial configuration and let free to evolve with time. Our emphasis has been to capture the three-stages of bubble coalescence, namely (a) collision, (b) squeezing out of the liquid until the film has reached a critical thickness, and (c) rupture of this thin film to form a coalesced bubble. Therefore, we have done simulations for an inline arrangement of bubbles without any initial random perturbation in the lateral positions. Figs. 8 and 9 show two such cases in which the current methodology has been used to study bubble coalescence in a 2-D fully periodic domain of size. 100 × 300. Fig. 8 shows the flow situation for two bubbles at $Eo = 53.7$ and $Mo = 0.297$ separated by an initial separation distance of 2.5d and Fig. 9 is at $Eo = 29.6$ and $Mo = 0.279$ with an initial separation of 2.0d, where 'd' is the initial diameter of the bubble. The preliminary cases were run with two bubbles, whose line connecting the centers is parallel to the gravitational vector. One of the objectives was to study the influence of the wakes left by the upper bubble(s), which subsequently move downstream into the path of the lower bubble(s). It can be observed that for bubbles with an Eotvos number of 53.7, the upper bubble deforms much more than the lower rising bubble. This can be explained by the fact that the upper bubble flows 'through' the quiescent liquid, while the lower one is traveling 'into' the wake left behind the upper bubble. Thus, the wake left behind by the upper bubble results in lower drag for the lower bubble. Since the relative velocity of the bubbles is non-zero, the distance between the two bubbles keeps decreasing with time. Eventually the bubbles touch/collide (see Figs. 8a and 9a), and soon after form a larger bubble with twice the volume as the initial bubble. The shape of this intermediate larger bubble (see Figs. 8b and 9b), at the time when the thin liquid film separating the two bubbles has just ruptured, is different for the two cases shown here, thereby indicating that bubble coalescence and behavior is a function of the Eotvos number and is not the same for all situations. In this case, Eotvos number was changed by changing the size of the initial bubble(s). Eventually at steady state, the bubble streamlines and the shapes for the two cases are found to be much different as was expected (see Figs. 8c and 9c). Simulations were also done for cases with more than two bubbles, aligned vertically and also in a staggered manner. For in-line bubbles, the motion of the bubbles is purely rectilinear. This can be explained as the initial bubble distribution has an axis of symmetry that runs through the center of

the bubbles, as can be seen in Fig. 10. So the bubbles do not experience lateral force and hence do not deviate in the lateral direction. The coalescence process of these bubbles is captured in Fig. 10c–g. It can be observed that the uppermost bubble flowing upstream into the path of the falling liquid has the maximum shape deformation, because of the highest drag experienced by this vapor phase. Fig. 10g shows an instance when some liquid is trapped inside the bubble after the bubble collision. This is due to high inertia at the time of impact, so the liquid is unable to squeeze out completely in time through the narrow gap left between the two bubbles, thus getting trapped inside the vapor phase. Eventually, as can be seen in Fig. 10h, the liquid 'pops' out from the bottom surface of the vapor. This phenomenon has also been observed by Takada et al. [24].

To study how the wakes behind the bubbles affect the motion of the downstream bubbles, a new simulation was run with three bubbles of the same size that are staggered by a lateral distance of the order of the initial diameter of the bubbles with respect to the gravitational vector. The simulation domain was chosen fairly long in the direction of rise of the bubbles (150 by 400; $d = 30$) so that the periodicity of the wake had minimal influence on the top-most bubble. The results of this test are shown in Figs. 11–13. The time for each snapshot is also mentioned, which has been non-dimensionalized using $\bar{t} = \sqrt{d_e/g}$. It was observed that as the bubbles move, the wake behind the upper bubbles creates an artificial lift force for the downstream bubbles, thereby causing the bubbles to move in a helical path. The effect of the lift force is such that the bubble shapes are no more oblate elliptical, rather change to oval-like. These oval bubbles seem to follow each other, into the wake left by the upstream vapor. Eventually these bubbles coalesce and the shape of the coalesced bubble is shown in Fig. 13a and b. The vortices for the two cases of rectilinear and helical bubble motion are also compared in Fig. 14. The shape of the vortex at either end of the major axis of the bubble is much different in both cases, and explains the helical path of the bubbles in the oscillatory motion of the wake.

4. Conclusions

The lattice Boltzmann method has been used in the current study to simulate single- and two-phase fluids. Benchmark studies were conducted to validate the code. Shan–Chen's interaction model has been used to simulate gravity driven two-phase flows. Bubble dynamics has been studied with single dispersed vapor

bubble in a heavier liquid, and the results show that the bubble shapes fall into the shape-chart created by Bhaga and Weber [2]. Simulation of bubbles with different sizes shows that as the Eotvos number increases, the bubbles deform from a spherical to oblate ellipsoid to disk-like and eventually at very high Eotvos numbers to skirt-like structures. Bubble drag calculations have also been done and the results have been found to compare well with existing empirical correlation of [2] and potential flow solution of [32]. Simulations done using LBM indicate the presence of the well-known phenomenon of hindered rise for spherical bubbles and cooperative rise for highly deformed bubbles.

Multiple bubbles are also simulated in large periodic domains and bubble coalescence characteristics are studied for different initial size and distances of the bubbles. Bubble coalescence was found to occur in a three stage process, namely collision, draining of the liquid film and eventually its rupture. It is observed that as the Eotvos number increases, the uppermost bubble deforms the most because of the maximum drag that it experiences from the liquid flowing downstream. The bubble dynamics is dictated by vortex pattern of the leading bubble, which allows the bubbles to coalesce. Such simulations have also been run for different configurations of the initial bubble distribution to show the effect of vortex shedding on the oscillatory motion of the bubbles. Staggered bubbles yield a qualitative overview of the process of bubble coalescence in channels in which lift forces come into play because of the presence of walls. Future work is directed towards the study of bubble nucleation and coalescence to form vapor slugs due to wall heating.

References

[1] J.R. Grace, Shapes and velocities of bubbles rising in infinite liquids, Trans. Inst. Chem. Eng. 51 (1973) 116–120.
[2] D. Bhaga, M.E. Weber, Bubbles in viscous liquids: shapes, wakes and velocities, J. Fluid Mech. 105 (1981) 61–85.
[3] R. Kumar, Two-phase flow microstructures in thin geometries: Multi-field modeling, in: M. Faghri, B. Sunden (Eds.), Heat and Fluid Flow in Microscale and Nanoscale Structures, WIT Press, Boston, 2004, pp. 173–224.
[4] G. Ryskin, L.G. Leal, Numerical solution of free-boundary problems in fluid mechanics. Part 2. Buoyancy-driven motion of a gas bubble through a quiescent liquid, J. Fluid Mech. 148 (1984) 19–35.
[5] A. Esmaeeli, G. Tryggvason, Direct numerical simulations of bubbly flows. Part 1. Low Reynolds number arrays, J. Fluid Mech. 377 (1998) 313–345.
[6] A. Esmaeeli, G. Tryggvason, Direct numerical simulations of bubbly flows. Part 2. Moderate Reynolds number arrays, J. Fluid Mech. 385 (1999) 325–358.
[7] K. Sankaranarayanan, X. Shan, I.G. Kevrekidis, S. Sundaresan, Analysis of drag and virtual mass forces in bubbly suspensions using an implicit formulation of the lattice Boltzmann method, J. Fluid Mech. 452 (2002) 61–96.
[8] U. Frisch, B. Hasslacher, Y. Pomeau, Lattice gas automata for the Navier–Stokes equations, Phys. Rev. Lett. 56 (1986) 1505–1508.
[9] S. Succi, The Lattice Boltzmann Equation for Fluid Dynamics and Beyond, first ed., Oxford University Press, Oxford, 2001. pp. 17–39.
[10] G. McNamara, G. Zanetti, Use of the Boltzmann equation to simulate lattice gas automata, Phys. Rev. Lett. 61 (1988) 2332–2335.
[11] D.R. Noble, S. Chen, J.G. Georgiadis, R.O. Buckius, A consistent hydrodynamic boundary condition for the lattice Boltzmann method, Phys. Fluids 7 (1) (1995) 203–209.
[12] S. Chen, G.D. Doolen, Lattice Boltzmann method for fluid flows, Ann. Rev. Fluid Mech. 30 (1998) 329–364.
[13] D. Rothman, J. Keller, Immiscible cellular-automaton fluids, J. Stat. Phys. 52 (1988) 1119–1127.
[14] D. Grunau, S. Chen, K. Eggert, A lattice Boltzmann model for multiphase fluid flows, Phys. Fluids A 5 (1993) 2557–2562.
[15] X. Shan, H. Chen, Lattice Boltzmann model for simulating flows with multiple phases and components, Phys. Rev. E 47 (1993) 1815–1819.
[16] S. Hou, X. Shan, Q. Zou, G.D. Doolen, W.E. Soll, Evaluation of two lattice Boltzmann models for multiphase flows, J. Comput. Phys. 138 (1997) 695–713.
[17] Z.L. Yang, T.N. Dinh, R.R. Nourgaliev, B.R. Sehgal, Numerical investigation of bubble growth and detachment by the lattice Boltzmann method, Int. J. Heat Mass Transfer 44 (2001) 195–206.
[18] T. Lee, P.F. Fischer, Eliminating parasitic currents in lattice Boltzmann equation method for non-ideal gases, Phys. Rev. E 74 (2006) 046709.
[19] M. Swift, W. Osborne, J. Yeomans, Lattice Boltzmann simulation of nonideal fluids, Phys. Rev. Lett. 75 (1995) 830–833.
[20] T. Inamuro, S. Tajima, F. Ogino, Lattice Boltzmann simulation of droplet collision dynamics, Int. J. Heat Mass Transfer 47 (2004) 4649–4657.
[21] T. Inamuro, T. Ogata, F. Ogino, Numerical simulation of bubble flows by the lattice Boltzmann method, Future Generat. Comput. Syst. 20 (2004) 959–964.
[22] T. Lee, C.-L. Lin, A stable discretization of the lattice Boltzmann equation method for simulation of incompressible two-phase flows at high density ratio, J. Comput. Phys. 206 (2005) 16–47.
[23] H.W. Zheng, C. Shu, Y.T. Chew, A lattice Boltzmann model for multiphase flows with large density ratio, J. Comput. Phys. 218 (2006) 353–371.
[24] M. Takada, M. Misawa, A. Tomiyama, S. Hosokawa, Simulation of bubble motion under gravity by lattice Boltzmann method, J. Nucl. Sci. Technol. 38 (5) (2001) 330–341.
[25] I.O. Kurtoglo, C.L. Lin, Lattice Boltzmann simulation of bubble dynamics, Numer. Heat Transfer B 50 (2006) 333–351.
[26] J.M. Buick, C.A. Greated, Gravity in a lattice Boltzmann model, Phys. Rev. E 61 (2000) 5307–5320.
[27] S. Chen, D. Martinez, R. Mei, On boundary conditions in the lattice Boltzmann method, Phys. Fluids 8 (1996) 2527–2536.
[28] P. Yuan, L. Schaefer, Equations of state in a lattice Boltzmann model, Phys. Fluids 18 (2006) 042101.
[29] X. Shan, Analysis and reduction of spurious currents in a class of multiphase lattice Boltzmann models, Phys. Rev. E 73 (2006) 047701.
[30] A. Tomiyama, Struggle with computational bubble dynamics, Multiphase Sci. Technol. 10 (1998) 369–405.
[31] I. Zun, Transition from wall void peaking to core void peaking in turbulent bubbly flow, in: Proceedings of ICHMT Conference on Transport Phenomena in Multiphase Flow, Dubrovnik, Yugoslavia, 1987.
[32] D.D. Joseph, Rise velocity of a spherical cap bubble, J. Fluid Mech. 488 (2003) 213–223.
[33] K. Sankaranarayanan, S. Sundaresan, Lift force in bubbly suspensions, Chem. Eng. Sci. 57 (2002) 3521–3542.
[34] O.C. Jones Jr., N. Zuber, The interrelation between void fraction fluctuations and flow patterns in two-phase flow, Int. J. Multiphase Flow 2 (1975) 273–306.
[35] K. Mishima, T. Hibiki, Flow regime transition criteria for upward two-phase flow in vertical narrow rectangular ducts, in: 3rd International Conference on Multiphase Flow, ICMF98, Lyon, France, 1998.